Chapter 4

Methodology

4.1 Introduction

The multi-phase field method developed by Steinbach et al. [33, 36] is employed in this study to develop a stand-alone model for intercritical annealing of low-carbon steels. Sub-models for ferrite recrystallization, austenite formation and austenite to ferrite transformation are developed. Neither bainitic nor martensitic transformation is taken into account in the present work. A parallel computer code is developed and implemented on computer clusters for phase field simulations. The models are first tuned and validated with experimental data from a systematically experimental study on intercritical annealing of a low-carbon steel by Kulakov [2]. The chemistry of the studied steel is listed in Table 4.1. The steel was cold-rolled with a thickness reduction of 50% using a laboratory mill and consists of 86% ferrite plus 14% pearlite. Moreover, the developed phase field model is used to study cyclic phase transformations in a plain-carbon steel and a Mn-alloyed low-carbon steel, which is validated with experimental data provided by Chen [86].

Table 4.1: Key alloying elements in the investigated steel (wt.%) [2].

C	Mn	Cr	Si
0.105	1.858	0.340	0.157

4.2 Basics of the Multi-phase Field Model

In the multi-phase field model [33,36], each microstructural constituent i, e.g. a grain, is represented by a phase field variable ϕ_i. The value of the phase field variable represents the local fraction of the relevant constituent. Inside the constituent i, the value of ϕ_i is 1 while the values of other phase field variables $\phi_j(j \neq i)$ are 0. The interface is a mixture of various constituents, i.e. more than one phase field variable is between 0 and 1. The sum of all phase field variables is one, i.e.:

$$\sum \phi_i = 1 \tag{4.1}$$

The phase field equations which describe the pair-wise interaction of adjacent constituents are given by:

$$\frac{\partial \phi_i}{\partial t} = \sum_{i \neq j} m_{ij} \left\{ \sigma_{ij} I_{ij} + \frac{\pi}{\eta} \sqrt{\phi_i \phi_j} \Delta G_{ij}^{driv} \right\} \tag{4.2}$$

with

$$I_{ij} = \left[\left(\phi_j \nabla^2 \phi_i - \phi_i \nabla^2 \phi_j \right) + \frac{\pi^2}{2\eta^2} \left(\phi_i - \phi_j \right) \right] \tag{4.3}$$

where I_{ij} is a curvature term, m_{ij} and σ_{ij} are the interface mobility and energy, ΔG_{ij}^{driv} is the driving pressure for interface migration and η is the

interface thickness. The interface thickness η is a numerical parameter which is usually larger than the physical thickness.

The mobilities are assumed to obey an Arrhenius relationship, i.e.:

$$m_{ij} = m_{ij}^0 exp \left(\frac{Q_{ij}^m}{RT} \right) \tag{4.4}$$

where R is the ideal gas constant, T is the temperature, m_{ij}^0 is the pre-factor and Q_{ij}^m is the activation energy.

Solute diffusion occurs during austenite formation and the austenite-to-ferrite transformation in low-carbon steels. In the present study, it is assumed that only the interstitial, i.e. carbon, can redistribute by long-range diffusion, which is described by:

$$\frac{dC^C}{dt} = \sum_i \left(\nabla \left(D_i^C \phi_i \nabla C_i^C \right) \right) \tag{4.5}$$

where D_i^C is carbon diffusivity in phase i, C_i^C is the carbon concentration in phase i and C^C is the local carbon concentration. The carbon diffusivity D_i^C obeys an Arrhenius relationship given by:

$$D_i^C = D_i^{C0} exp \left(-Q_i^C / RT \right) \tag{4.6}$$

where D_i^{C0} is the pre-factor and Q_i^C is the activation energy (Table 4.2). Given the local carbon concentration C^C, the phase carbon concentration C_i^C is calculated based on the following equations:

$$\frac{C_i^C}{C_j^C} = \frac{C_i^*}{C_j^*} \tag{4.7}$$

and

$$C^C = \sum_i \left(\phi_i C_i^C \right) \tag{4.8}$$

where C_i^* is the para-equilibrium carbon concentration. The para-equilibrium phase diagram (Fig. 4.1) is calculated with Thermo-Calc®(TCFE7 database).

Table 4.2: Carbon-diffusion parameters [13].

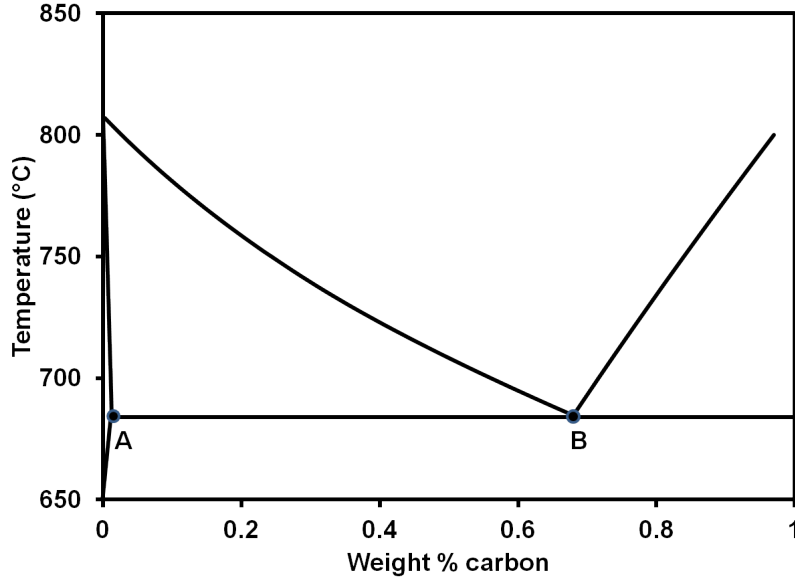| Phase	Pre-factor (m^2/s)	Activation energy (kJ/mol)
Ferrite	2.2×10^{-4}	122.5
Austenite	0.15×10^{-4}	142.1

Figure 4.1: Para-equilibrium phase diagram for the studied steel.

4.3 Numerical Techniques

The phase field equations (Eq. 4.2) and diffusion equations (Eq. 4.5) are non-linear partial differential equations (PDEs). The finite difference method is used to solve the PDEs in a discretized computational domain. The computational domains used in this study are square in 2D and cubic in 3D. Thus the domain is simply discretized into a Cartesian grid having the same grid spacing Δx in all directions (Fig. 4.2).
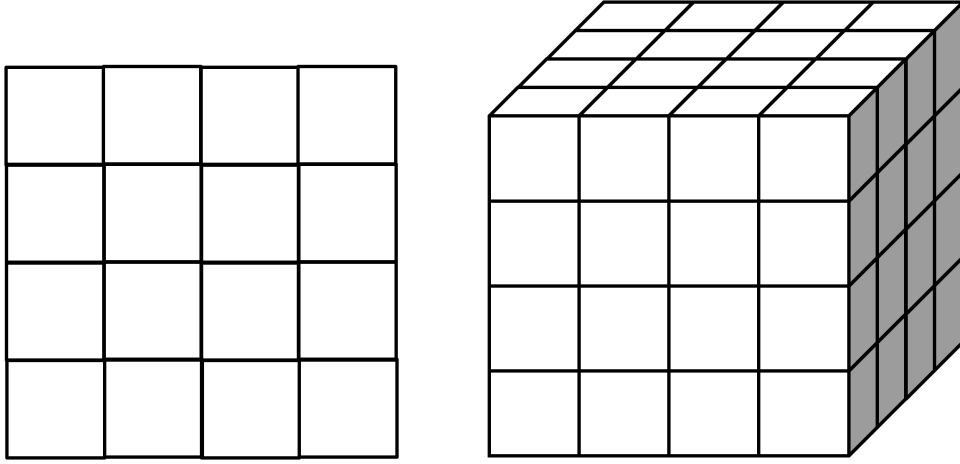

Figure 4.2: Schematic of the grid structure in the computational domain.

A sparse data structure is used to store variables on each grid point, including the indice and values of non-zero phase field variables as well as local solute concentrations. The detailed description of the data structure can be found elsewhere [20].

Centered finite difference with the nearest neighbors (5-point stencil in 2D and 7-point stencil in 3D) is used to discretize the first and second derivatives. For example, the gradient and Laplacian of ϕ at grid point (i, j, k) in a 3D

domain are given by:

$$\nabla \phi_{i,j,k} = \frac{\partial \phi_{i,j,k}}{\partial \mathbf{n}} = \left(\frac{\phi_{i+1,j,k} - \phi_{i-1,j,k}}{2\Delta x}, \frac{\phi_{i,j+1,k} - \phi_{i,j-1,k}}{2\Delta x}, \frac{\phi_{i,j,k+1} - \phi_{i,j,k-1}}{2\Delta x} \right)$$

(4.9)

and

$$\nabla^2 \phi_{i,j,k} = \frac{\partial^2 \phi}{\partial x^2} + \frac{\partial^2 \phi}{\partial y^2} + \frac{\partial^2 \phi}{\partial z^2}$$

$$= \frac{\phi_{i+1,j,k} + \phi_{i-1,j,k} + \phi_{i,j+1,k} + \phi_{i,j-1,k} + \phi_{i,j,k+1} + \phi_{i,j,k-1} - 6\phi_{i,j,k}}{\Delta x^2}$$

(4.10)

The Forward Euler method is used to implement the integration in the time domain for both phase field and diffusion equations, e.g.

$$\left(\frac{\partial \phi_i}{\partial t} \right)^t = \frac{\phi_i^{t+\Delta t} - \phi_i^t}{\Delta t}$$

(4.11)

where Δt is the time step, ϕ_i^t is the current value of ϕ_i, $\phi_i^{t+\Delta t}$ is the value for the next time step. The Forward Euler method is conditionally stable and the time step has to fulfill the following requirement:

$$\Delta t < \Delta t_c = min \left(\frac{\Delta x^2}{2 Dim \cdot max \left(m_{ij} \sigma_{ij} \right)}, \frac{\Delta x^2}{2 Dim \cdot max \left(D_i^C \right)} \right)$$

(4.12)

where Dim is the domain dimensionality. For simplicity, the time step is represented by $\Delta t = \xi \Delta t_c$ where the factor ξ is adjusted between 0 and 1 to

compromise between computational cost and numerical accuracy.

Suitable values of the other numerical parameters, i.e. the grid spacing Δx and the interface thickness η represented by the number of grid points, i.e. $n_\eta \Delta x$, have to be chosen based on both computational cost and accuracy. Convergence and accuracy analyses were carried out to select appropriate values for the three parameters, i.e. n_η, Δx and ξ. The details are discussed in Chapter 5 and Chapter 6.

4.4 Initial Microstructures

The initial microstructures used in the phase field simulations (Chapter 5-7) are constructed using a modified Voronoi tessellation [136,137], based on the experimental data, e.g. the average ferrite grain size, the rolling reduction, the phase fractions and pearlite-band spacing. Periodic boundary conditions are applied. In the 2D simulations of cyclic phase transformation (Chapter 8), micrographs are used directly as the initial microstructures. In this case, insulate boundary conditions are used, i.e. $\frac{\partial \phi_i}{\partial \mathbf{n}} = 0$ where $\mathbf{n}$ denotes the normal to the boundary, because periodic boundaries are not applicable to real microstructures.

4.5 Ferrite Recrystallization

The recrystallization model considers ferrite recrystallization only and microstructure evolution in pearlite, e.g. spheroidization, is not taken into account at this stage. The stored energy mainly in the form of dislocations,

as the driving force for recrystallization, is an input of the phase field model. The stored energy in the present study is assumed to be an attribute of grains and uniform within each grain. The calculation of stored energy in the investigated cold-rolled steel is discussed in Chapter 5.

In this model, the physical process of nucleation from substructures is not considered. Rather, the nuclei are introduced to the simulation domain as spherical grains. Nuclei can grow rather than shrink only if the initial size is larger than a critical value, i.e. $2\sigma_{ij}/\Delta g_v$ where σ_{ij} is the interface energy and Δg_v is the driving force for nucleation. For phase transformations, the critical size is usually on nanoscale and below the grid spacing used for mesoscale simulations. In this case, an initial size equal to the grid spacing Δx is appropriate. But for recrystallization, because the driving force is usually 1-2 orders of magnitude smaller than phase transformation, the critical size of nuclei is about 0.1-1 μm, similar to the grid spacing used in mesoscale simulations. Thus, the critical size is used as the initial size of an nucleus for recrystallization. Site-saturated nucleation is assumed such that all nucleation events occur effectively at the beginning of recrystallization. The nuclei density is based on the average ferrite grain size after full recrystallization. The spatial distribution of nuclei is defined by a rule that all nuclei are distributed randomly among those grains having a stored energy higher than a critical value E^{st*}, i.e.

$$E^{st} > E^{st*} \tag{4.13}$$

where E^{st*} is an adjustable parameter, the value of which is calibrated with the experimentally measured recrystallization kinetics.

The driving pressure ΔG_{ij} for recrystallization in Eq. 4.2 is given by:

$$\Delta G_{ij} = E_j^{st} - E_i^{st} \tag{4.14}$$

where E_i^{st} and E_j^{st} are the stored energy in grain i and j, respectively. The stored energy in recrystallized grains is assumed to be 0.

All ferrite grain boundaries are assumed to be high-angle grain boundaries. Thus, the interface energy and mobility are the same for all ferrite grain boundaries. The ferrite grain-boundary energy is set to 0.76 J/m² [49]. The grain-boundary mobility is kept adjustable and calibrated with the experimentally measured recrystallization kinetics. The details of tuning the adjustable parameters are discussed in Chapter 5.

4.6   Austenite Formation

In this sub-model, pearlite is assumed to be a pseudo phase, because it is a great challenge to model the lamellar structure with a characteristic length of 100 nm when considering microstructures on a scale of 10-100 μm. The carbon concentrations in both pearlite and ferrite are set to the para-equilibrium eutectoid compositions, i.e. 0.68 wt% and 0.012 wt% (point A and B in Fig. 4.1), while the other substitutional elements are assumed to be uniformly distributed in the microstructure.

Savran et al. [96] conducted dedicated studies on austenite nucleation and observed continuous nucleation in a low-carbon steel. These results are in qualitative agreement with the observations by Kulakov [2] in the steel investigated here. Similar to previous observations, Kulakov found rapid

pearlite-to-austenite transformation followed by a more gradual transformation of ferrite to austenite. Further, austenite nucleation was observed to occur at both pearlite/ferrite interfaces and ferrite grain boundaries. Thus, two separate nucleation models are postulated for two different nucleation sites.

Site saturation is assumed for austenite nucleation at pearlite/ferrite interfaces with a nuclei density that is, based on the experimental observation [138], approximately independent of heating scenarios. A nuclei density of 0.024 μm^{-2} [138] is adopted and the nucleation temperature is set to 730 °C, in agreement with the measured start temperature of austenite formation at the lowest investigated heating rate, i.e. 1°C/s [2].

The classical nucleation theory is employed to describe the more gradual austenite nucleation at ferrite grain boundaries:

$$\frac{dN}{dt} = \lambda N_n(t) exp \left(-\frac{\frac{\Psi}{\Delta g_V^2} + Q_\alpha^{Fe}}{k_B T} \right) \qquad (4.15)$$

where k_B is the Boltzmann constant, λ is a constant related to the atom jump frequency, $N_n(t)$ is the number of potential nucleation sites that is proportional to the total length of ferrite grain boundaries in the 2D simulation domain and decreases with time t as more and more nuclei occupy the ferrite grain boundaries, Ψ is a constant related to the assumed nucleus shape and interface properties (2.1×10^{-6} J^3/m^6 [139]), Q_α^{Fe} is the activation energy of iron diffusion in ferrite (3.9×10^{-19} J [96]), and Δg_V is the driving force for nucleation which depends on the temperature and the average carbon concentration in ferrite (the carbon concentration gradient in ferrite is presumably negligible due to the high diffusivity and low solubility)

which is calculated with Thermo-Calc$^{®}$. The factor λ is kept adjustable and calibrated with the experimental data. In the case of concurrent ferrite recrystallization and austenite formation, it is assumed that the migrating recrystallization fronts are not potential nucleation sites.

Further, it was observed that austenite grains formed at ferrite grain boundaries grow mainly into one of the two neighboring ferrite grains [97]. This observation can be rationalized based on special crystallographic orientation relationships between the austenite grain and one of the adjacent ferrite grains, e.g. the Kurdjumov-Sachs (K-S) relationship, making this portion of the α/γ interface semi-coherent and of low mobility. In the present model, it is postulated that all the austenite nuclei at a boundary segment between two ferrite grains α_1 and α_2, have a special orientation relationship with one specific ferrite grain (e.g. α_1) but not with the other one (α_2), such that the mobility of the α_1/γ interface is 1% of that of the α_2/γ interface, leading to dominant growth of austenite grains into α_2. It is a random selection in the model as to whether α_1 or α_2 is the grain with which austenite has a special orientation relationship. The nuclei are introduced into the simulation domain as spherical grains with a radius of the grid spacing Δx.

As pearlite is a pseudo phase, the following postulations are made: (1) no carbon diffusion is considered in pearlite; (2) pearlite interacts with austenite only; (3) transformation of pearlite to austenite is assumed to be interface controlled with a driving force of:

$$\Delta G_{P\gamma}^{driv}(T) = G_P(T) - G_\gamma(T) \tag{4.16}$$

where the Gibbs free energies of pearlite G_P and austenite G_γ are evaluated

with Thermo-Calc®. Because pearlite is not a phase but a mixture of ferrite and cementite, its free energy is calculated from:

$$G_P = x_\alpha G_\alpha(T) + (1 - x_\alpha)G_\theta(T) \tag{4.17}$$

where x_α is the molar fraction of ferrite in eutectoid pearlite; G_α and G_θ are the molar Gibbs free energy for ferrite and cementite, respectively. The Gibbs free energy of austenite and ferrite in Eq. 4.16 and 4.17 is calculated with constant carbon concentrations of 0.68wt% and 0.012wt%, respectively.

The chemical driving pressure for the ferrite-to-austenite transformation is described by:

$$\Delta G_{\alpha\gamma}^t = \chi_{\alpha\gamma}(T) \left(C_\gamma^C - C_\gamma^* \right) \tag{4.18}$$

where $\chi_{\alpha\gamma}(T)$ is a proportionality factor that is calculated with Thermo-Calc® (Appendix A), C_γ^C is the interfacial carbon concentration in austenite and C_γ^* is the para-equilibrium carbon concentration in austenite. The stored energy in a deformed ferrite grain is included in the driving pressure at the interfaces between the deformed ferrite grain and its neighboring austenite grains.

Further, the solute drag effect due to trans-interface diffusion of the main substitutional alloying element, i.e. Mn, is taken into account using the Gibbs-energy dissipation model by Hillert [75] . Therefore, the effective driving pressure for the ferrite/austenite interface migration $\Delta G_{\alpha\gamma}^{eff}$ in the phase field equations (Eq. 4.2) is given by:

$$\Delta G_{\alpha\gamma}^{eff} = \Delta G_{\alpha\gamma}^{t} - \Delta G_{\alpha\gamma}^{diss} \qquad (4.19)$$

where $\Delta G_{\alpha\gamma}^{diss}$ is the dissipated Gibbs-energy that is calculated with the Gibbs-energy dissipation model as described in Section 4.7.

The γ/P interface energy is 0.9 J/m^2 [113] and the γ/α interface energy is 0.4 J/m^2 [13]. The γ/P and γ/α interface mobilities are adjusted to fit the experimentally measured transformation kinetics. The details of fitting the adjustable parameters in the present sub-model are discussed systematically in Chapter 6.

4.7 Gibbs-energy Dissipation Model

In the present study, the solute-drag effect on phase transformations is modeled using the Gibbs-energy dissipation theory by Hillert [75]. A wedge-shaped interaction potential of Mn across an α/γ interface is used (Fig. 2.6). Assuming quasi-steady-state diffusion of Mn across an α/γ interface (Eq.2.16) and no long-range diffusion in the bulk, the concentration profile of Mn $x^{Mn}(y)$ across an interface moving with a velocity of V is described by [77]:

$$\frac{x^{Mn}}{x_0^{Mn}} = \frac{V' + a\exp\left(-\left(V' + a\right)\left(Y + 1\right)\right)}{V' + a}$$
$$if -1 \leq Y \leq 0$$

$$\frac{x^{Mn}}{x_0^{Mn}} = \frac{V' + \left(\frac{a(V'+b)}{(V'+a)}\exp\left(-\left(V' + a\right)\right) + \frac{(b-a)V'}{(V'+a)}\right)\exp\left(-Y\left(V' + b\right)\right)}{(V' + b)}$$
$$if \, 0 \leq Y \leq 1 \tag{4.20}$$

where x_0^{Mn} is the molar fraction of Mn in the bulk and :

$$Y = \frac{y}{\Lambda} \tag{4.21}$$

$$V' = \frac{V\Lambda}{D_{int}^{Mn}} \tag{4.22}$$

$$a = (\Delta E - E_0)/RT \tag{4.23}$$

$$b = (\Delta E + E_0)/RT \tag{4.24}$$

Here, E_0 is the binding energy to the interface, $2\Delta E$ is the difference of chemical potentials in austenite and ferrite which is calculated with Thermo-Calc®, D_{int}^{Mn} is the trans-interface diffusivity of Mn, and 2Λ denotes the physical interface thickness which is different than the 'numerical' interface thickness η in the phase field equation. A schematic of the Mn concentration profile across an α/γ interface is shown in Fig. 4.3.
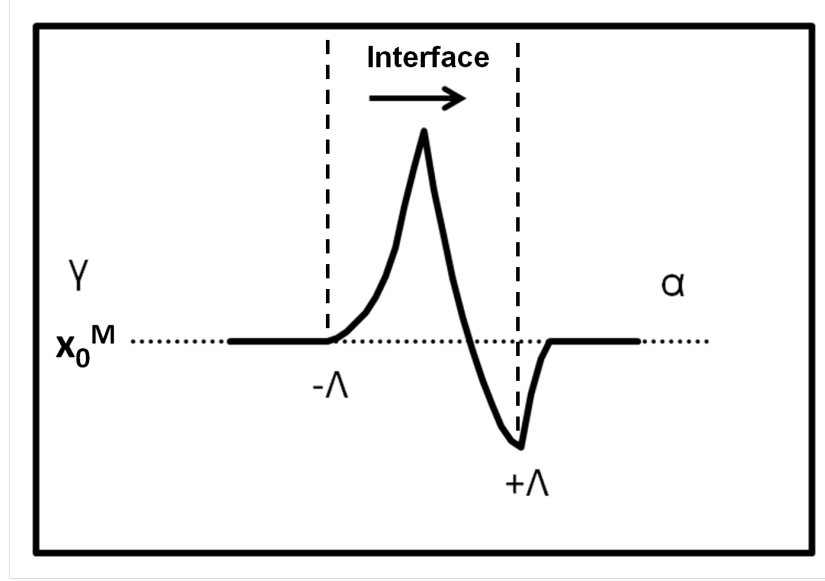
Figure 4.3: Illustration of the Mn concentration across an α/γ interface for the ferrite-to-austenite transformation: a negative spike is formed in front of the α/γ interface.

The dissipated Gibbs-energy (Eq. 2.18) is given by :

$$
\begin{aligned}
\Delta G_{\alpha\gamma}^{diss} \;=\; & -x_0^{Mn} RT/V_m \{ \frac{a^2}{V+a} \left[-1 + \frac{1 - exp\left(-V - a \right)}{V+a} \right] + \qquad (4.25)\\
& \frac{b}{V+b} \left[\left(b - a\left(V + b \right) \frac{1 - exp\left(-V - a \right)}{V + a} \right) \frac{1 - exp\left(-V - b \right)}{V+b} - b \right] \}
\end{aligned}
$$

where V_m is the molar volume of the iron matrix.

The present Gibbs-energy dissipation model considers two effects of the trans-interface diffusion of Mn on the α/γ interface [75]. One effect is a change of the chemical driving pressure. The chemical driving pressure eval-
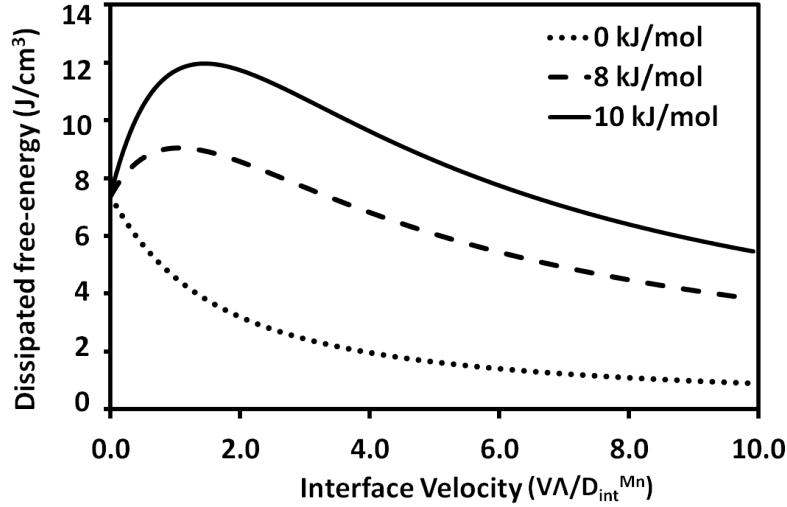
Figure 4.4: Dissipated Gibbs-energy by trans-interface diffusion of Mn across an α/γ interface at 770 °C for a low-carbon steel (0.1wt%C-1.86wt%Mn) with different binding energies.

uated using Eq. 4.18 is under the condition of an identical Mn concentration on both sides of the α/γ interface. However, the actual Mn concentrations on two sides of the interface, i.e. Mn concentrations at $-\Lambda$ and $+\Lambda$ in Fig. 4.3, are unequal due to the trans-interface diffusion. Thus, the chemical driving force is changed and the change is taken into account by the dissipated Gibbs-energy (Eq. 4.25). The other effect is a solute drag effect which exists only on a moving interface in case the binding energy is nonzero. If the binding energy is 0, the dissipated Gibbs-energy account for the first effect only, i.e. the change of chemical driving force. Fig. 4.4 shows the variation of dissipated Gibbs-energy with different interface velocities and binding energies. The nonzero dissipated Gibbs-energy for a zero binding energy demonstrates the first effect of trans-interface diffusion.

The dissipated Gibbs-energy in the present model is nonzero at a stationary interface $\Delta G_{\alpha\gamma,0}^{diss}$ (Fig. 4.4). Based on Eq. 4.25, the dissipated Gibbs-energy at a stationary interface is given by:

$$\Delta G_{\alpha\gamma,0}^{diss} = -x_0^M RT/V_m \left(1 - \frac{2\Delta E}{RT} - exp\left(\frac{2\Delta E}{RT}\right)\right) \qquad (4.26)$$

which is independent of the binding energy.

Assuming the effective driving pressure is 0 in Eq. 4.19, the interfacial carbon concentration C_γ^C at a stationary interface is:

$$C_\gamma^C = C_\gamma^* + \frac{\Delta G_{\alpha\gamma,0}^{diss}}{\chi_{\alpha\gamma}(T)} \qquad (4.27)$$

which implies that if Gibbs-energy dissipation is considered, the thermodynamic equilibrium at a stationary interface is not para-equilibrium but negligible-partitioning local equilibrium (NPLE) [81]. Based on the present model assumptions, the para-equilibrium interface condition can exist only at a fast moving interface in case Gibbs-energy dissipation is negligible.

Because Gibbs-energy dissipation occurs at a stationary interface, the positive chemical driving pressure could be smaller than the nonzero dissipated Gibbs-energy at a stationary interface, leading to a negatively effective driving pressure. In this case, the effective driving pressure is forced to 0 and thus the interface will remain stationary until the chemical driving pressure becomes larger than the dissipated Gibbs-energy.

The value of Λ is assumed to be 0.5 nm [85]. The binding energy is assumed to be 10 kJ/mol [86]. The trans-interface diffusivity of Mn is assumed to be the geometrical average of bulk diffusivities in ferrite and austen-

ite [84, 140], i.e.

$$D_{int}^{Mn} = 0.5 \times 10^{-4} exp\left(-\frac{247650}{RT}\right) m^2/s \qquad (4.28)$$

In order to integrate the Gibbs-energy dissipation model with the phase field model, the interface velocity in the Gibbs-energy dissipation model (Eq. 4.25) is further expressed with the phase field variable ϕ_i :

$$V = |\frac{\partial \mathbf{n}}{\partial t}| = \frac{\partial \phi_{\mathbf{i}}}{\partial t}/|\frac{\partial \phi_{\mathbf{i}}}{\partial \mathbf{n}}| \qquad (4.29)$$

where $|\frac{\partial \phi_{\mathbf{i}}}{\partial \mathbf{n}}|$ is given by Eq. 4.9.

4.8 Austenite-to-ferrite Transformation

In the cooling process of an intercritical annealing cycle, austenite will transform back to ferrite partially by reversing the moving direction of austenite/ferrite interfaces without ferrite nucleation, which is termed epitaxial ferrite growth. The formulations proposed for austenite formation in Section 4.6 and Section 4.7 are used for epitaxial ferrite growth, e.g. calculation of the driving pressure and solute drag pressure. The austenite/ferrite interface mobility and energy are also kept the same.

By integrating the models of ferrite recrystallization, austenite formation and austenite-to-ferrite transformation, a stand-alone phase field model is developed that can describe all aspects of microstructure evolution during an entire intercritical-annealing cycle. The developed model is also applied to modeling the cyclic phase transformation in Chapter 8.

4.9   Grain Growth

Grain growth of both ferrite and austenite is included in the phase field model. The interface energy and mobility of the ferrite grain boundary are set in the recrystallization sub-model (Section 4.5). The austenite-grain-boundary energy is taken to be 0.7 J/m^2 [10]. The activation energy of the austenite-grain-boundary mobility is taken to be 185 kJ/mol [10] and the pre-factor is adjusted such that the average austenite grain sizes after full austenitization for various heating scenarios are consistent with the experimental measurements.

4.10   Model Implementation

Both FORTRAN and C/C++ are used as the programming language to translate the phase field model into a computer program. The code is parallelized using OpenMP and MPI (Message Passing Interface) libraries and also accelerated with GPU (Graphics Processing Unit) computing. The implementation of the program is schematized in Fig. 4.5. First, input files containing the necessary data, e.g. domain size, phase diagram, interface properties and thermal paths, are read by the program. Then an initial microstructure is constructed using Voronoi tessellation or input from a file alternatively. The main body of the program is a series of time loops in which nucleation models and solvers of phase field equations and diffusion equations are implemented. In each loop, the values of model parameters are updated, e.g. time, temperature and solute diffusivity. Selected data can be written to disk as specified by the user. Once the condition of termination
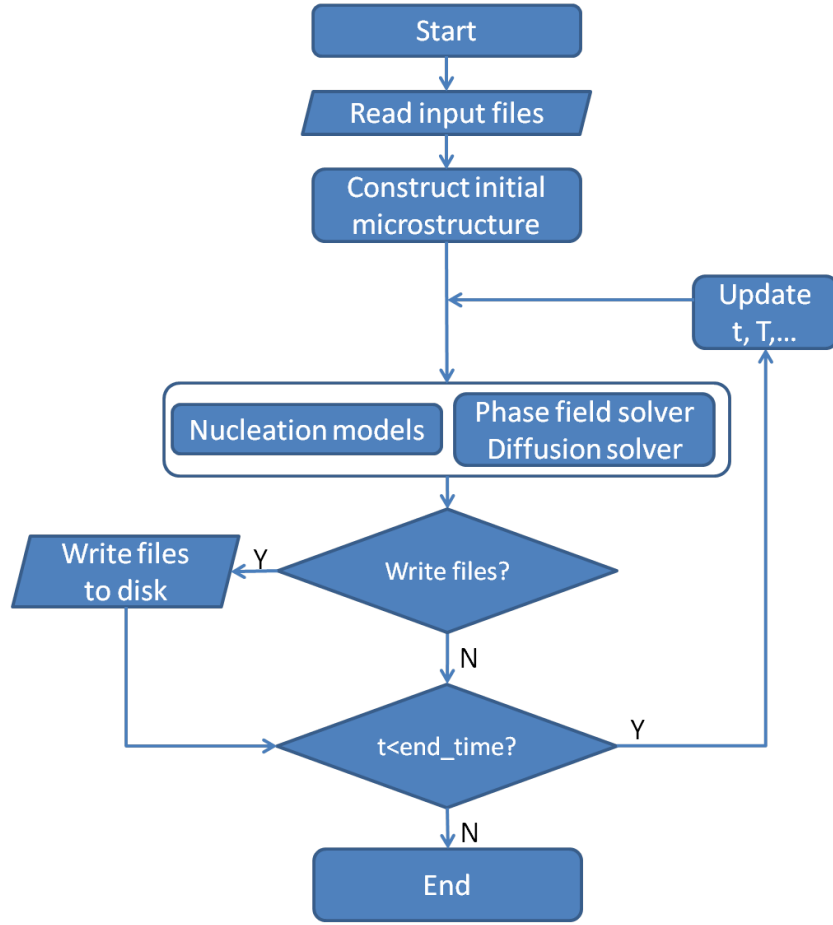
Figure 4.5: Flowchart of the model implementation.

is met, the program stops.

Both phase field and carbon concentration field are written to files and visualized with the software ParaView®. Other statistical information is also exported by the program, e.g. recrystallized ferrite fraction, austenite fraction and grain sizes. The equivalent diameter is used as the grain size [2]. In order to compare with the grain sizes measured using 2D micrographs, various 2D cuts of the 3D domain are used to calculate grain sizes.